

Quantum LSTM Model for Estimation of Energy Expenditure in Human Aging using Wearable IoT Healthcare Technology

Bao-Nhi Dang Tran, *Student Member, IEEE*, Muhammad Fahim, *Member, IEEE*, Bradley D. E. McNiven, *Member, IEEE*, Mohsen Guizani, *Fellow, IEEE*, Hyundong Shin, *Fellow, IEEE*, and Trung Q. Duong, *Fellow, IEEE*

Abstract—Physical activity energy expenditure (PAEE) offers significant benefits for general healthcare monitoring and has the potential to promote healthy and active aging for elderly individuals. With recent advancements in quantum information and computation, quantum machine learning (QML) has emerged as a tool capable of improving upon the measurement of PAEE. In this paper, we propose a hybrid QML model to predict PAEE which consists of a classical long short-term memory (LSTM) model integrated with a variational quantum circuit (VQC). This model, which we refer to as the enhanced quantum long short-term memory linear (eQLSTML), was subsequently trained and tested using the publicly available GTOV Human Physical Activity and Energy Expenditure Dataset for Older Individuals. In particular, we study the proposed eQLSTML model with different gate choices in the quantum circuit along with various embedding and layering techniques. Our results indicate our model to be superior in both performance comparisons and prediction when compared to traditional machine learning methods currently employed. Our findings indicate that combining QML approaches with wearable IoT healthcare devices provides a new avenue for personalized healthcare monitoring and an effective method for promoting healthy aging.

Index Terms—Internet-of-Things (IoT), IoT Healthcare, Quantum Machine Learning, eHealth.

I. INTRODUCTION

Preserving health and functional mobility is paramount for maintaining a high quality of life, especially from the

B.-N. D. Tran and B. D. E. McNiven are with the Faculty of Engineering and Applied Science, Memorial University, St. John's, NL A1B 3X5, Canada (e-mail: {ntrandangbao, b.mcniven}@mun.ca

M. Fahim is with Queen's University Belfast, UK, (e-mail: m.fahim@qub.ac.uk).

M. Guizani is with the Machine Learning Department, Mohammad Bin Zayed University of Artificial Intelligence, Abu Dhabi, UAE (e-mail : mguizani@ieee.org).

H. Shin is with the Department of Electronic Engineering, Kyung Hee University, Yongin-si, Gyeonggi-do 17104, South Korea (e-mail: hshin@khu.ac.kr).

T. Q. Duong is with the Faculty of Engineering and Applied Science, Memorial University, St. John's, NL A1C 5S7, Canada, and with the School of Electronics, Electrical Engineering and Computer Science, Queen's University Belfast, BT7 1NN Belfast, U.K., and also with the Department of Electronic Engineering, Kyung Hee University, Yongin-si, Gyeonggi-do 17104, South Korea (e-mail: tduong@mun.ca).

This paper has been presented in part at the International Conference on Quantum Communications, Networking, and Computing (QCNC'24), Kanazawa, Japan, July 2024.

This work was supported in part by the Canada Excellence Research Chair (CERC) Program CERC-2022-00109. The work of H. Shin was supported by the National Research Foundation of Korea (NRF) grant funded by the Korean government (MSIT) under RS-2025-00556064 and by the MSIT (Ministry of Science and ICT), Korea, under the Convergence security core talent training business support program (RS-2023-00266615) supervised by the IITP (Institute for Information & Communications Technology Planning & Evaluation).

perspective of healthy aging. This principle has garnered much attention and has since led to the establishment of the Institute of Aging by the Canadian Institution of Health Research as a part of the Government of Canada's commitment to promoting healthy and independent lives for senior citizens while preserving the quality of life in all health statuses. Similarly, the UN Decade of Healthy Aging is an international initiative established to improve the lives of older individuals through strategies that promote age-friendly environments, combat ageism, and ensure access to quality healthcare tailored to the needs of the aging population. While these are just two of many efforts aimed at addressing the challenges associated with an aging population, several obstacles remain persistent in achieving healthy aging [1]–[3]. For example, a significant challenge is the prevalence of multimorbidity, the coexistence of multiple chronic conditions, among older adults, which complicates health management and the maintenance of functional mobility. Recent studies have indicated that multimorbidity affects physical function and further complicates health management in older populations, leading to higher rates of functional disability and additional challenges to mobility and independence [4], [5].

To date, there have been an increasing number of studies demonstrating how regular moderate-intensity exercise in older populations can significantly reduce the risk of infectious and cardiovascular diseases, as well as mortality [6]–[8]. One of the key factors shown to promote physical activity of individuals is the quantification and monitoring of physical activity energy expenditure (PAEE) [9]–[11]. Previous work has indicated that indirect calorimetry, measured through wearable accelerometer sensors, is an effective method for estimating PAEE [12]. More specifically, the combination of accelerometer data with physiological measurements (i.e., heart monitoring) can provide reasonable estimations on PAEE through linear and non-linear modeling methods such as random forest regressors and deep learning methods like artificial and convolutional neural networks [13], [14].

Interestingly, estimating PAEE from accelerometer data has been primarily performed on young and middle-aged populations [13], [15], making existing methods less suitable for older populations who have different energy requirements, expenditure patterns, and activity levels [16]–[19]. Additionally, older adults are on average more sedentary in comparison to younger individuals [20], resulting in the need for a simpler PAEE model that is less computationally intensive but sufficient enough to make accurate predictions.

In recent years, the fields of quantum technology and information have seen significant developments in hardware and algorithms [21], [22]. One such development has been the emergence of quantum machine learning (QML), which leverages properties of quantum systems like superposition and entanglement to solve complex computational problems that were previously deemed intractable. One technique within QML of particular value is the variational quantum circuit (VQC) [23], which is a hybrid algorithm with tunable parameters optimized through classical algorithms. This approach has since been applied to various problems, some of which include energy time-series forecasting [24], [25], DNA classification [26], and predictions in electroencephalogram abnormalities [27]. Notably, there has been a recent development of a quantum-based Long Short-Term Memory (QLSTM) model for time-series data with variational quantum circuits (VQCs) replacing classical neural layers; introduced first in 2022 by Chen et al. [28]. Similarly, Ceschini et al. presented a fully quantum implementation of LSTM cells on quantum hardware, aiming at accelerating computation and enhancing scalability for quantum neural networks [29]. Additionally, Yu et al. demonstrated a hybrid QLSTM approach incorporating VQCs for solar irradiance prediction, achieving superior accuracy compared to classical forecasting methods [25]. Another study by Lin et al. showed that their Quantum-Train LSTM significantly reduces the number of trainable parameters in flood prediction tasks, highlighting the viability of quantum methods for large-scale parameter reduction, albeit with a noted trade-off in predictive accuracy [30]. Furthermore, Chehimi et al. explored federated QLSTM (FedQLSTM) frameworks, enabling distributed quantum learning for temporal data and substantially reducing communication overhead, thereby paving the way for scalable and privacy-preserving quantum machine learning applications [31].

These pioneering studies have significantly influenced this research as they demonstrate foundational insights into the potential and practical implementation strategies of quantum-enhanced LSTM models. Inspired by these advancements, quantum computing is particularly suitable for modeling subtle temporal variations and intricate feature interactions often present in healthcare sensor data, specifically in the context of physical activity energy expenditure (PAEE) estimation. While classical deep learning methods are powerful, they probably encounter challenges in accurately capturing nuanced data patterns critical for precise predictions in older populations. In contrast, quantum-enhanced machine learning leverages quantum properties such as entanglement and interference to better represent and explore these complex temporal correlations [32], [33], thus positioning quantum computing as a compelling approach to enhance predictive accuracy and computational efficiency in PAEE monitoring for older adults. Motivated by these promising findings, this paper aims to explore the potential of QLSTM methodologies in the healthcare domain, which can leverage advantages to improve predictive performance on healthcare-related time-series data, such as forecasting physical activity energy expenditure (PAEE). In this work, we propose a novel hybrid linear quantum long

short-term memory model and explore different embedding techniques and VQC configurations to optimally forecast PAEE in older individuals. The main contributions of this paper include:

- The design of an enhanced-quantum Long Short-Term Memory model with a linear embedding layer, which we refer to as eQLSTML, which utilizes data preprocessing to predict the PAEE for older individuals.
- Exploration and implementation of different quantum encoding techniques and associated discussion surrounding the implementation of QML for processing raw time series biosignal sensor data.
- Investigation of VQCs with strongly entangled CRX gates and circuit block connectivity patterns for better expressibility and stronger entanglement.
- Application of a separate embedding layer before and after each VQC block to improve the learning ability for non-linear problems.

The paper is organized as follows: Section I presents the introduction, motivation, and main contributions of this study. Section II reviews related works relevant to this research. Section III describes the dataset, including an overview of the data, details about data collection procedures, and specifications of devices and locations involved. Section IV outlines the feature engineering process, specifically focusing on data transformation and sequential data preparation. Section V provides comprehensive background knowledge about quantum computing and the classical LSTM model as a basis for subsequent discussions. Section VI details the proposed model's framework, introduces the linear embedding layer with adjustments made for our implementation, explains the rationale behind our selected configuration, and describes the proposed model architecture, implementation details, optimization methods, evaluation metrics, and training approaches. Section VII presents experimental results along with detailed analyses, comparisons, and discussions. Finally, the paper concludes with Section VIII.

II. RELATED WORKS

In recent years, various methods for estimating PAEE in younger populations have been developed, with models ranging from simple linear regression to more complex machine-learning approaches. Montoye *et al.* [13] presented a comprehensive comparison of multiple methods which included linear regression, linear mixed models, and artificial neural networks (ANNs) using data from 40 participants, aged between 18 and 44 years old, who wore sets of four accelerometers while performing various physical activities. The measurements were recorded by a portable metabolic analyzer connected to a breathing mask. It was found that the ANN models generally outperformed the studied linear models in terms of correlation and root mean squared error (RMSE), particularly when accelerometers were placed on the wrists.

Similarly, Ellis *et al.* [34] developed a random forest regressor (RFR), which involved using data, collected from wearable accelerometers and a portable indirect calorimeter, from 40 participants (average age 35.8) performing household

and locomotion activities during a six minute period. RFR was compared to a previously developed ANN model created in [35] and was shown to perform favorably by producing a lower RMSE, which was further amplified when including data associated with participant heart rate and data from wrist and hip accelerometers. An additional study by Zhu *et al.* [36] introduced a convolutional neural network (CNN) for PAEE estimation using data from a cohort of 30 participants with an average age of 27.8 years old. Throughout a time period of 30 minutes, each participant performed six activities of various intensity both inside and outside while equipped with a triaxial accelerometer device on the waist and a portable indirect calorimetry device to record participant's heart rate. This model, which automatically extracted features from the accelerometer data, yielded the best results when compared to the previously mentioned linear regression and ANN models in terms of RMSE across several activity types, however, still struggled in capturing the long-term dependencies in sequential data, which is essential for accurately modeling PAEE from triaxial accelerometer data.

Although QML approaches have not yet been applied to PAEE data, their use in time series data in healthcare fields has increased dramatically in recent years due to their effectiveness in processing large, high-dimensional datasets, which classical techniques commonly struggle with. For instance, VQCs and quantum neural networks (QNNs) have been employed to predict states of mind based on electroencephalogram (EEG) signals during neuromarketing experiments involving like/dislike decisions [37]. Moreover, the quantum k-means algorithm was applied to cluster groups based on demographic and laboratory measurement data to predict heart disease [38]. In terms of treatment effectiveness, QNNs have been used to forecast knee arthroplasty outcomes, leveraging clinico-demographic data from more than 150 patients over two years of treatment. Additionally, different types of QNNs, including continuous-variable models, have been applied to COVID-19 time series data to optimize population-level measurements [39]. These models, although demonstrated the success of quantum approaches in processing complex time series data, are primarily focused on classification tasks and do not fully address the complexities of sequential data found in PAEE estimation.

III. DATASET

In this work, we analyze sensor-based experimental data from wearable technology obtained from the Growing Old Together Validation (GOTOV) study accessible through the 4TU data repository [40], [41]. The data includes both indirect calorimetry measurements and accelerometer data collected from various body locations, such as the ankle and wrist.

A. Overview

The GOTOV study consists of 35 individuals (14 females, 21 males), mainly from Leiden, Netherlands, aged between 60 and 85 years old. The statistical overview of participant-level data is shown in Table I.

In total, participants engaged in 16 different indoor and outdoor activities over a timeframe of 90 minutes. Indoor activities included resting postures (i.e., sitting and standing), stair climbing, and household chores, while outdoor activities included a variety of exertion levels, such as walking at different paces and cycling. It is noted that only 25 participants were involved in outdoor activities due to weather limitations.

TABLE I: Statistical information collected from participants while performing 16 different activities. SD - standard deviation, EEm - energy expenditure measurement, BMI - body mass index, BR - breathing rate.

	Mean	SD
Age (years)	65.7	5.0
Height (cm)	174.5	7.9
Weight (kg)	83.1	11.5
BMI (kg/m)	27.2	2.7
EEm (Kcal)	3.8	1.1
BR (s)	0.31	0.04

B. Devices and locations

Fig. 1 presents the set of devices used and their relative placement on each participant of the study. As shown in the figure, this included an accelerometer and additional sensors to measure physiological signals like oxygen consumption, carbon dioxide production, breathing rate, and heart rate. We note that in this paper, we restrict our focus to data coming from accelerometers and indirect calorimetry.

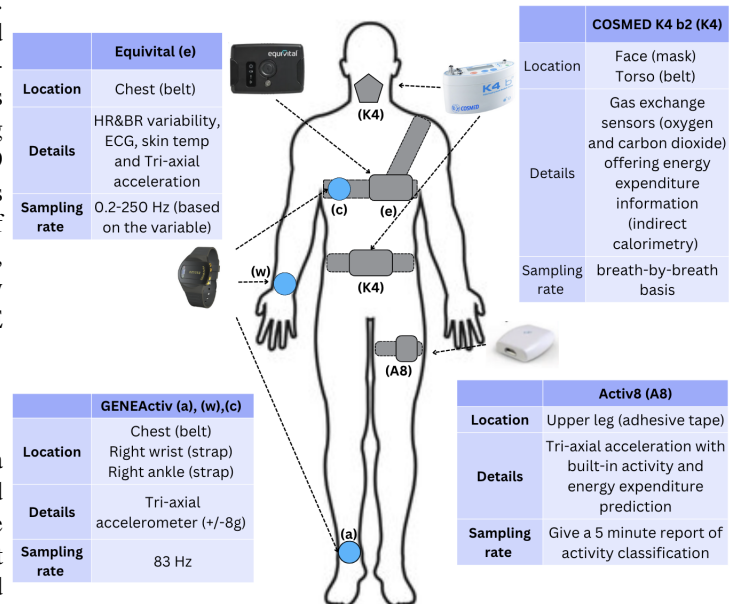


Fig. 1: Depiction of device placement for participants in the study. In total, four different devices were used in six body locations including the face, torso, chest, wrist, ankle, and upper leg.

Ankle and wrist-worn GENEActiv accelerometers captured the activity levels and movement patterns of the participants. These accelerometers recorded triaxial acceleration data within

an expected uncertainty of ± 8 g and a sampling rate of 83 Hz. Sample data from each accelerometer axis (ankle and wrist) is shown in Figure 2.

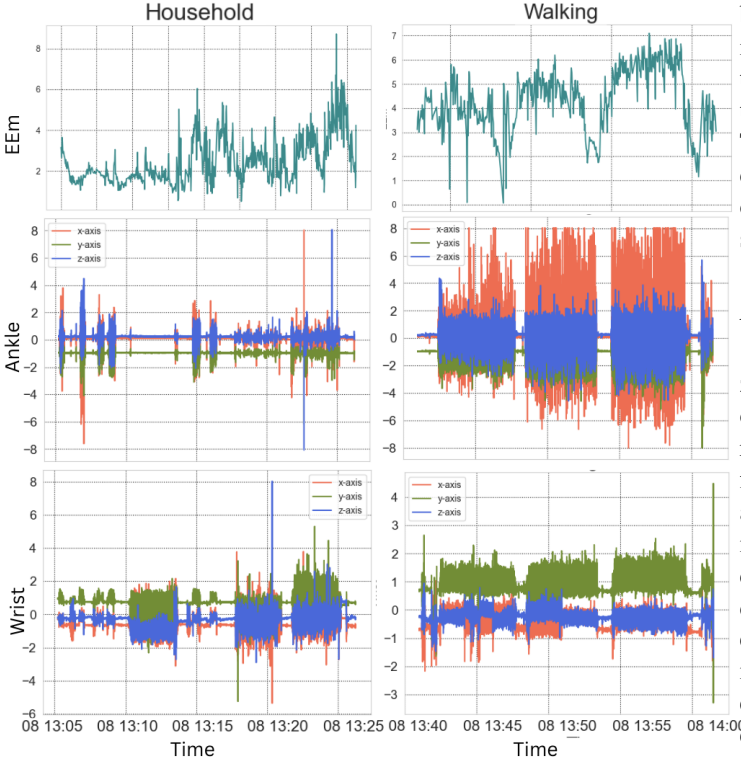


Fig. 2: Example showing raw data measured from ankle and wrist devices for household and walking.

Indirect calorimetry measurements were performed using a COSMED K4b2 system [42] which measured breath-by-breath volumes of oxygen (O_2) and carbon dioxide (CO_2) throughout the performed activities. The system included a mask connected to a portable unit that housed O_2 and CO_2 analyzers, barometric sensors, and processing electronics. These analyzers produced the measurement for O_2 , and CO_2 exchange, allowing for the calculation of the energy expenditure measurement (EE_m), along with metabolic equivalents. The EE_m output served as our target variable for our PAEE modeling in the model training and testing sections. Notably, the sampling rate of this signal matched participant breathing rates, resulting in a variable sampling rate averaging around 0.3 Hz.

IV. FEATURE ENGINEERING

To construct our model for PAEE estimation, it is essential to transform the predictor (accelerometer) and target (EE_m) data. Specifically, the transformations normalize the data through the use of a downsampling rate for target and input data, followed by the construction of an appropriate sequence for model training and evaluation.

A. Target downsampling

As mentioned previously, the COSMED system measures energy expenditure per breath, which resulted in a variable

sampling rate that reflects the participant's breathing patterns (see Fig. 2). Therefore, to address this variability and create a fixed sampling rate suitable for training machine learning models, the downsampled COSMED signal is assumed to be an effective resolution. The chosen target sampling rate is 0.1 Hz, meaning within each window we could calculate the mean EE_m value to create a new data point representing the average energy expenditure over that 10-second interval. This downsampling approach avoids generating more training data during periods of higher breathing, while also smoothing out occasional outlier EE_m values measured by the COSMED system.

B. Standardize input data

As a first step, the target and numeric predictor data were z-normalized to have zero mean and a standard deviation of 1. This ensures both data consistency and quality while removing any inconsistencies. Furthermore, this ensures these features are on a comparable scale, leading to a more robust and interpretable model, resulting in a fairer evaluation of model performance [43], [44]. In addition, data normalization can mitigate potential bias arising from features with vastly different scales, resulting in an improved convergence rate and enhancing the stability of the model [45]. It also facilitates more effective comparisons between predictive targets by ensuring each contributes equally to the analysis, thereby enhancing interpretability [46].

C. Building sequence

The training process of general recurrent neural network (RNN) modeling requires sequence data, and the LSTM technique is a special type of RNN. Therefore, the input data from the accelerometers will be transformed into sequences, where each sequence is linked to a single EE_m value. In this study, each sequence captures the sensor data measured at the moment leading up to a given EE_m value in a specific window time with a defined length of the sequence (i.e., the number of inputs) and resolution (i.e., sampling rate), therefore, the training process of the RNN model used in this study requires transforming accelerometer signal data into specific sequences. This involves the determination of three key factors:

- The sequence length (L_s): the number of data points included in each sequence that will be used during the training and testing process (i.e., RNN sequence size).
- The window length (L_w): defines the actual time duration that the sequence represents.
- Resolution/sampling rate (R): this determines the frequency that data captures within the window, and is equal to the ratio between L_s and L_w .

In simple terms, within the same window size, the more data points used in the sequence (i.e., longer sequence size), the lower the sampling rate needed to maintain. Crucially, L_w needs to be long enough to capture the influence of past activities on energy expenditure. In this work, we use the most optimal combination of sequence length of 50 for the window length of 2 minutes with a down-sampling rate of 0.417 Hz.

To synchronize predictor data to the expected sequence and window lengths, we downsample the accelerometer data to a specific sample rate. This downsampling aggregates multiple data points into a single value. While several aggregation approaches exist, such as using the mean or other statistical dispersion aggregations, in this work we employ the standard deviation method. The standard deviation has been shown to effectively capture the variation in movement within the GO-TOV dataset [14], making it the optimal choice for aggregation in our preprocessing stage.

V. FOUNDATIONS OF QUANTUM COMPUTING

A. Quantum bits, Gates and Circuits

In classical computation, the fundamental unit of information that is manipulated, operated, and stored is called a bit and is assigned a state of either 0 or 1. Quantum computation, however, relies on a quantum bit (i.e., qubit) and can exist in both of these states simultaneously via a superposition [47]. This general state can be defined as

$$|\psi\rangle = \alpha|0\rangle + \beta|1\rangle \quad (1)$$

where α and β are the probability amplitudes of the $|0\rangle$ and $|1\rangle$ states, respectively, such that $|\alpha|^2 + |\beta|^2 = 1$. Furthermore, quantum gates are used to perform basic operations on these qubits and are defined as unitary matrices. Below we introduce the specific gates used in this work:

Rotation gates: are operators that rotate the state of a given qubit around the x-, y-, or z-axis of the Bloch sphere. Thus, these rotation gates are angle (ϕ) dependent and are represented as:

$$R_x(\phi) = \begin{pmatrix} \cos(\frac{\phi}{2}) & -i \sin(\frac{\phi}{2}) \\ -i \sin(\frac{\phi}{2}) & \cos(\frac{\phi}{2}) \end{pmatrix}, \quad (2)$$

$$R_y(\phi) = \begin{pmatrix} \cos(\frac{\phi}{2}) & -\sin(\frac{\phi}{2}) \\ \sin(\frac{\phi}{2}) & \cos(\frac{\phi}{2}) \end{pmatrix}, \quad (3)$$

$$R_z(\phi) = \begin{pmatrix} e^{-i\frac{\phi}{2}} & 0 \\ 0 & e^{i\frac{\phi}{2}} \end{pmatrix}. \quad (4)$$

Controlled-not (CNOT) gate: is a basic two-qubit quantum gate widely used in quantum computing to generate quantum entanglement. It operates on a pair of qubits, where one qubit acts as the control and the other as a target. The function of the CNOT gate is to flip the state of the target qubit, and its matrix representation can be defined as:

$$\text{CNOT} = \begin{pmatrix} 1 & 0 & 0 & 0 \\ 0 & 1 & 0 & 0 \\ 0 & 0 & 0 & 1 \\ 0 & 0 & 1 & 0 \end{pmatrix}, \quad (5)$$

where the first two rows correspond to the control qubit in state $|0\rangle$ while the last two rows correspond to it in the state $|1\rangle$. This means that if the control qubit is in $|1\rangle$, the target qubit flips its state (i.e., 0 becomes 1 and vice-versa).

Otherwise, the target qubit remains unchanged. We note that while the CNOT gate is an effective and simple technique to create entanglement, it also has limitations. Since CNOT gates do not allow for full connection between all pairs of qubits, the resulting entanglement between qubits is relatively weak. Consequently, this limited entanglement leads to the reduction of the circuit's ability to fully exploit quantum correlations, hence hindering model learning ability. The absence of sufficient qubit interactions impairs the model's capacity to explore complex quantum states, ultimately affecting its overall expressibility.

CRZ gate: To enhance the expressibility of the quantum circuit, a more advanced rotational gate controlled-Z gate was applied by Cao et al [25], which offered a better ability to control state evolution in their QLSTM model. The CRZ gate is a two-qubit gate that applies a rotation around the z-axis of the target qubit if the control qubit is in the $|1\rangle$ state. The CRZ gate is defined as:

$$\text{CRZ}(\theta) = \begin{pmatrix} 1 & 0 & 0 & 0 \\ 0 & 1 & 0 & 0 \\ 0 & 0 & e^{-i\frac{\theta}{2}} & 0 \\ 0 & 0 & 0 & e^{i\frac{\theta}{2}} \end{pmatrix} \quad (6)$$

The most significant drawback of the CRZ gate is commutative, limiting its ability to explore diverse quantum state space [48].

CRX gate: Similar to the CRZ gate, the CRX gate is a two-qubit operation that applies an x-axis rotation on the target qubit if the control qubit is in the $|1\rangle$ state. This introduces significantly better flexibility in quantum state manipulation in comparison to the CRZ gate, as unlike the CRZ gate, it is not commutative. Additionally, CRX gates allow for a broader exploration of the quantum state space, improving both the expressibility and the entangling capability of the quantum circuit [48], [49]. The CRX gate is mathematically expressed as

$$\text{CRX}(\theta) = \begin{pmatrix} 1 & 0 & 0 & 0 \\ 0 & 1 & 0 & 0 \\ 0 & 0 & \cos(\frac{\theta}{2}) & -i \sin(\frac{\theta}{2}) \\ 0 & 0 & -i \sin(\frac{\theta}{2}) & \cos(\frac{\theta}{2}) \end{pmatrix} \quad (7)$$

The rotation angle θ allows for fine-tuned state transitions, which when combined with its ability to entangle qubits more effectively than the CRZ and CNOT gates, makes the CRX gate the optimal choice for variational layers in a quantum circuit [48]

B. VQCs

VQCs are quantum circuits with adjustable parameters that can be optimized iteratively through parametrized quantum gates [50]. In recent years, VQCs have gained growing attention due to their robustness against quantum noise in the ever-growing noisy immediate-scale quantum (NISQ) era [51]. To date, VQCs have been implemented in solving problems for a diverse range of areas, such as function approximation [23], quantum chemistry [52], generative modeling [53], and optimization [54]. Furthermore, other work has shown stronger expressive power of VQCs in comparison to classical neural

networks. Some noteworthy examples include the usage of a multi-parameterized quantum circuit as a simulator for probability distribution [55] and quantum annealing strategies coupled with entanglement methods in intractable classical problems [56]. More details surrounding VQC functionality and layer structure will be discussed in the following section.

C. Long Short-Term Memory

Long Short-Term Memory (LSTM) networks, introduced by Hochreiter and Schmidhuber in 1997 [57], is a special type of Recurrent Neural Network that was designated to tackle the issue of vanishing or exploding gradient encountered in traditional RNNs. This enables LSTM to capture and learn from long-range dependencies in sequential data like text, audio, and time series. LSTM has gained many achievements in a wide range of applications, especially in Natural Language Processing including machine translation [58], sentimental analysis [59], and time series classification [60]. Within LSTM architecture, at each time step, each LSTM unit incorporates an additional state called the *cell state* (denoted as c_t) which serves as long-term memory reservoir of the LSTM unit, allowing the gradient to flow unchanged (this is the key difference of LSTM compared to ordinary RNN that rely solely on the hidden state (denoted as h_t). The LSTM unit maintains the combination of cell state and hidden state to control state updates and generates the outputs. Concisely, the computation at time step t was defined by C.Olah [61] as follows:

$$f_t = \sigma(W_f \cdot [h_{t-1}, x_t] + b_f) \quad (8)$$

$$i_t = \sigma(W_i \cdot [h_{t-1}, x_t] + b_i) \quad (9)$$

$$\tilde{C}_t = \tanh(W_C \cdot [h_{t-1}, x_t] + b_C) \quad (10)$$

$$C_t = f_t \otimes C_{t-1} + i_t \otimes \tilde{C}_t \quad (11)$$

$$o_t = \sigma(W_o \cdot [h_{t-1}, x_t] + b_o) \quad (12)$$

$$h_t = o_t \otimes \tanh(C_t) \quad (13)$$

where: f_t , i_t , \tilde{C}_t , C_t , o_t , and h_t are the forget gate, input gate, cell input, cell state, output gate, and hidden state, respectively, at time step t . W_f , W_i , W_C , W_o are weight matrices, and b_f , b_i , b_C , b_o are bias vectors. x_t is the input vector at time step t . $[h_{t-1}, x_t]$ represents the concatenation of the previous hidden state h_{t-1} and the current input x_t . The σ denotes the sigmoid activation function, and \tanh denotes the hyperbolic tangent function. And the symbol \otimes represents an element-wise product (Hadamard product)

D. Quantum Long Short-Term Memory and linear enhanced layers

Quantum long-short memory (QLSTM) is a quantum-based version of the classical LSTM model where the key distinguishing factor is the replacement of VQCs in different gates in the circuit instead of classical neural networks. In QLSTM, the implementation of VQCs has been shown to play an essential role in the extraction of feature data and compression of data, along with accelerated learning ability and enhanced stability for convergence [28]. Fig. 3 illustrates the QLSTM structure

and the equation below displays its corresponding forward pass in a solid form:

$$v_t = [h_{t-1}, x_t] \quad (14)$$

$$f_t = \sigma(VQC_1(v_t)) \quad (15)$$

$$i_t = \sigma(VQC_2(v_t)) \quad (16)$$

$$\tilde{c}_t = \tanh(VQC_3(v_t)) \quad (17)$$

$$c_t = f_t \otimes c_{t-1} + i_t \otimes \tilde{c}_t \quad (18)$$

$$o_t = \sigma(VQC_4(v_t)) \quad (19)$$

$$h_t = VQC_5(o_t \otimes \tanh(c_t)) \quad (20)$$

$$y_t = VQC_6(h_t) \quad (21)$$

where t represents the time step; v_t represents the concatenation of the previous hidden state h_{t-1} , x_t . f_t , i_t , \tilde{c}_t , c_t , o_t , h_t , and y_t represent the forget gate, input gate, candidate cell state, cell state, output gate, hidden state, and output of the LSTM model, respectively. σ denotes the sigmoid and \tanh denotes the hyperbolic tangent, both are activation functions and \otimes represents an element-wise product (Hadamard product). $\{VQC_n\}$ are Variational Quantum Circuits that replaces classical neural network layer $n = (1, 2, 3, 4, 5, 6)$

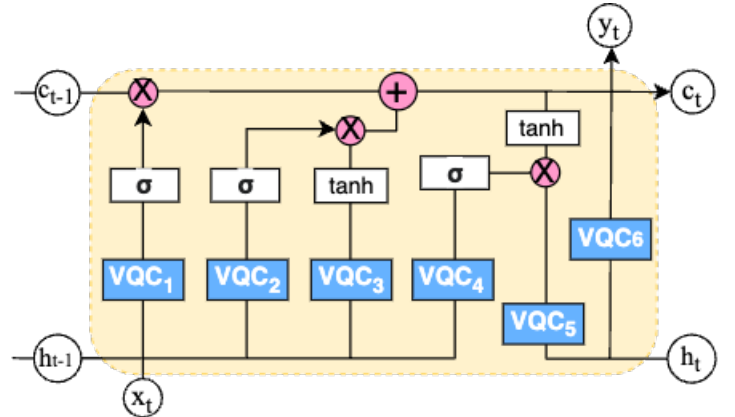


Fig. 3: Schematic depicting the insertion of VQCs into the classical LSTM network to form the QLSTM model.

VI. MODEL ARCHITECTURE

A. Framework

In this study, we propose a hybrid quantum-classical framework that utilizes an enhanced quantum long short-term memory linear (eQLSTML) model for predicting PAEE in elderly individuals, which we refer to as the eQLSTML model. Unlike traditional machine learning models, this framework distributes computational tasks between quantum and classical components. In this work, we use quantum computation to offload computationally intensive tasks, while classical computation is used to manage feature preprocessing, mapping, and parameter optimization. A dedicated data engineering module is also included to preprocess and transform accelerometer and calorimetry data into a form that is suitable for eQLSTML training.

The framework consists of multiple stages, which are illustrated in Fig. 4, including data preprocessing, model training,

and prediction. Initially, the data engineering module processes sensor data, such as normalizing and extracting features, and stores the preprocessed data in a database. During model training, classical neural networks compress the input features, which are then fed into VQCs. The VQC output is subsequently passed back to classical neural networks for PAEE prediction. The framework iteratively calculates and minimizes the error between predicted and true PAEE values using a gradient-based optimizer, which updates the parameters of both classical and quantum components until the result is converged. Once the model is fully trained, it can be used to provide real-time PAEE predictions to support activity monitoring and health management in older individuals.

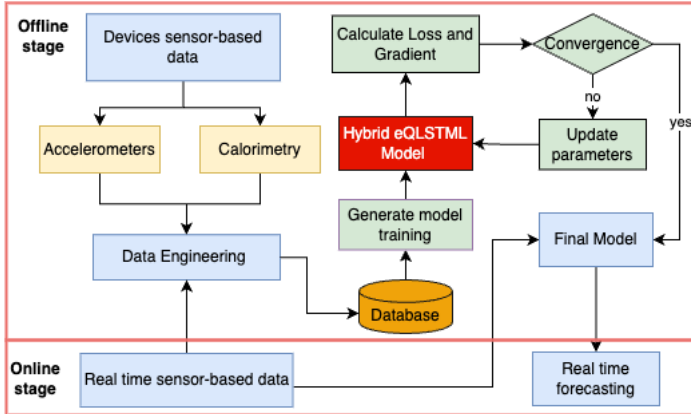


Fig. 4: Hybrid quantum computing based PAEE forecasting framework

B. Linear Embedding Layer

While QLSTM demonstrates effectiveness in time series forecasting with regular features, limitations arise due to qubit usage during the data encoding and compressing process. QLSTM uses a one-to-one mapping scheme that requires encoding both hidden states (with p hidden units) and input features (with q features) to use $(p + q)$ qubits in VQC. However, the output dimension needs to be matched with the hidden state of q units, which not only wastes quantum information for the remaining qubits during training but also leads to inefficient qubit usage that can hinder the model's learning capability. To combat this issue, a linear-layer embedding scheme was recently proposed which can significantly improve the QLSTM performance with effective usage of several qubits [25]. The linear embedding layer acts as a feature compressor, transforming input features from n dimensions into a target of m dimensions using matrix multiplication with $m \leq n$. The feed-forward pass formulation is shown as

$$z_{t_f} = L_{in}(q_t), z_{t_i} = L_{in}(q_t) \quad (22)$$

$$z_{t_u} = L_{in}(q_t), z_{t_o} = L_{in}(q_t) \quad (23)$$

$$f_t = \sigma(L_1(VQC1(z_{t_f}))) \quad (24)$$

$$i_t = \sigma(L_2(VQC2(z_{t_i}))) \quad (25)$$

$$\tilde{c}_t = \tanh(L_3(VQC3(z_{t_u}))) \quad (26)$$

$$c_t = f_t \otimes c_{t-1} + i_t \otimes \tilde{c}_t \quad (27)$$

$$o_t = \sigma(L_4(VQC4(z_{t_o}))) \quad (28)$$

$$h_t = o_t \otimes \tanh(c_t) \quad (29)$$

$$y_t = L_f(h_t) \quad (30)$$

where L_{in} is the linear embedding layer applied to the concatenated vector $q_t = [h_{t-1}, x_t]$, where h_{t-1} is the hidden state from the previous time step and x_t is the input at the current time step. The outputs of L_{in} , denoted as z_{tn} in which $n = (f, i, u, o)$, represent the compressed features for the forget, input, update, and output gates, respectively. Each z_{tn} is passed through (VQC_n) and a linear transformation layer (L_m) to produce the gate activations f_t, i_t, o_t , and the candidate cell state \tilde{c}_t with $\{L_m\}$ corresponding to the set of linear layers applied after VQCs' output $n = (1, 2, 3, 4)$, L_f is a representation of the linear layer in the final computation stage of the model to get the predicted value. Note that all VQC_n from 1 to 4, described here follow an identical conceptual design, structural logic, and implementation approach, which will be described in section C below, ensuring consistency throughout the proposed model.

Our proposed model takes into account this well-established embedding approach, but in different implementations as shown in Fig. 5. Specifically, our model employs separate feature embedding layers before and after each variational quantum layer. This contrasts with using a shared embedding layer before and a separate embedding layer after each VQC. These embedding layers function as feature maps, transforming the input data vector $q_t = [h_{t-1}, x_t]$, in which h_{t-1} represents the hidden state at the previous time step and x_t represents the current input into the compressed feature representation. This strategy of employing separate embedding layers allows for capturing non-linearities effectively and each layer can learn a distinct mapping specifically tailored to the corresponding VQC. This ultimately allows the model to better capture the intricacies of the data relevant to each quantum circuit. After the VQC layer, another separate embedding layer is used to map the VQC output to h_t . This preference stems from the analogy between VQCs in our proposed eQLSTM model gates within traditional LSTM. Similar to how distinct LSTM gates handle different functions, the implemented VQCs serve a specific purpose since a single, shared linear embedding layer would not be able to effectively extract diverse information tailored to the unique functionalities of each VQC. Consequently, employing separate linear embedding layers after the implementation of the VQCs proves to be a more

suitable approach, allowing the model to capture the nuances of the data relevant to each quantum circuit.

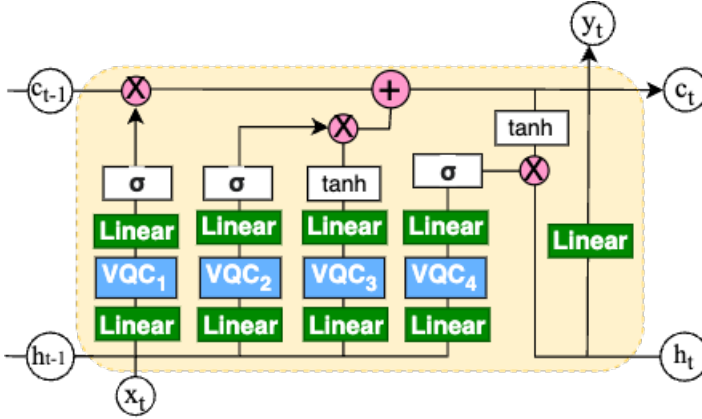


Fig. 5: Architecture of eQLSTM with separate embedding layer before and after each VQCs block.

C. VQC blocks

In this work, our quantum circuit consists of three specific VQC blocks as follows:

1. The Quantum Embedding Layer: Quantum embedding refers to the process of encoding classical data into its quantum representation and is done through a quantum feature map. This feature map acts as a translator that converts classical data into a set of gate parameters, which ultimately generate a corresponding quantum state. In this work, the exploration of various encoding methods will be conducted in order to identify the most effective approach. These include 2N rotation (2Nr) encoding, amplitude encoding, and angle embedding. [28], [62]

a) 2N Rotation Encoding

In the paper Quantum Long Short-Term Memory model [28], the encoding scheme transforms classical data input vectors into quantum states by utilizing a process that involves single-qubit rotations. Initially, the system uses Hadamard gates with the initial states to create an unbiased state, this makes the initial state become a uniform superposition state. The input is then transformed again into two rotation angles $R_y(\theta_{i,1})$ and $R_z(\theta_{i,2})$, where $\theta_{i,1} = \arctan(x_i)$ and $\theta_{i,2} = \arctan(x_i^2)$ which is applied to guide the corresponding rotation around the y-axis (using the Ry gates) and then later on by z-axis (using Rz gates) on the qubits. This encoding ensures that the classical input data is embedded into the quantum system as a quantum state, which is ready for subsequent processing by the quantum circuit. The authors chose the arctan function as it allows a wider range during the encoding process.

b) Amplitude Embedding

To further explore more efficient encoding techniques, we implemented amplitude encoding. Amplitude encoding will encode data as amplitudes of the quantum state, facilitating data manipulation more effectively while maintaining a lower number of qubits required. Specifically, let's consider a normalized classical data set with N-dimensions consisting of x

data points, which can be represented by the amplitudes of a qubit quantum state $|\psi_x\rangle$ in the below expression:

$$|\psi_x\rangle = \sum_{j=1}^M x_j |j\rangle \quad (31)$$

where $M = 2^n$, x_i is the j-th element of x, and $|i\rangle$ is the j-th state of computational basis.

For the dataset with P inputs and Q features, amplitude encoding encodes these features into a quantum state using only $n_{qubits} = \log_2 PQ$ qubits, along with the time of logarithmic in a number of data points, given an efficient algorithm. This encoding offers a significant advantage for quantum machine learning, where the manipulation of high-dimensional data with fewer qubits is enabled. Additionally, amplitude encoding also promises to exponentially speed up the training process because loading data (PQ features) takes time that grows linearly with the data size [63].

c) Angle Embedding:

In the final consideration, angle embedding is used, which is the most prevalent encoding approach because of its simplicity and high efficacy [62], [64]. In this encoding technique, the encoding process for classical input data x is done by single qubit rotation gates. Each element within the input vector determines the rotation angle of its corresponding gate, for example, Rx, Ry, or Rz rotation gates. This encoding method requires n qubits or more to encode n input variables. Mathematically, this relationship can be expressed as:

$$|\psi_x\rangle = \otimes_n R_m(x_i) |\psi_0\rangle \quad (32)$$

where x is the classical input, R_m is selected rotation matrix in which $m = x, y, z$.

2. The Variational Layer: This layer is responsible for qubit entanglement as well as the rotation of qubits. In this work, we explore the use of different rotational gates in the variational layer to compare their efficiency and determine the most effective one for our model. These gates include those described above, which include the CNOT, CRX, and CRZ gates.

3. The Connectivity Pattern Layer: The connectivity pattern between qubits is another vital aspect of the VQC architecture. Although we tested both near-block and all-to-all connectivity patterns, we chose the former in our final model as in this configuration the qubits are arranged in a natural way that forms a closed loop. More precisely, each circuit block within this structure incorporates sections of consecutive nearest-neighbor interactions complemented by a non-local interaction that establishes cyclic connectivity. This structure strikes a balance between computational efficiency and expressibility. Hence, establishing increasing connectivity that can possibly lead to stronger entangling capacity and more relatively favorable expressibility without the overhead of connecting every qubit to every other qubit, maintaining a lower cost of training in terms of circuit complexity and number of parameters [48]. In contrast, in all-to-all connectivity, each qubit can interact with all others in the circuit, maximizing the entangling capability and expressibility of the quantum circuit. Nonetheless, this comes at a cost of increased circuit depth, parameter count, and qubit connectivity requirements, which makes it more demanding for implementation on near-term

quantum hardware.

4. The Measurement Layer: In this layer, the measurement of each VQC block is performed after all other computational steps. In the proposed model, the measurement to be considered is computational basis state probabilities. Expectation values can be computed numerically on classical computers through quantum simulator software packages that offer zero-noise quantum computation. However, on real quantum devices, these values are typically estimated statistically through repeated measurements. The measurement process yields a fixed-length vector and will be further processed by the classical computer for prediction purposes.

D. Proposed VQC Architecture For Current Task

As we explore various techniques in both the embedding and variational layers, we propose a VQC architecture combining angle embedding and CRX gates. The reason for this selection is based on comprehensive studies mentioned earlier in Section VI.C and Section V.A. Angle embedding was selected because of its proven efficiency and simplicity, providing more effective quantum state representation, as demonstrated in recent studies [62], [64]. Furthermore, the choice of CRX gates was motivated by their superior entangling capabilities and expressibility compared to CRZ and CNOT gates [48], [49] in line with previous research highlighting their effectiveness in quantum circuit learning tasks [25].

This combination is paired with a near-block connectivity pattern in the variational layer, called strongly entangled controlled-X, which is illustrated in Fig. 6. These techniques have been selected based on their demonstrated superior performance in our preliminary experiments, particularly for temporal data modeling tasks. The angle embedding allows for flexible and efficient data encoding, while the presence of the CRX gates provides enhanced entangling capabilities and a larger space. Together, these components contribute to a model that improves upon the original QLSTM and LQSTM architectures, ultimately offering better expressibility, lower training costs, and higher accuracy for temporal data modeling tasks. The overall strengths of the proposed model are comprehensively evaluated and discussed in the next section of our paper.

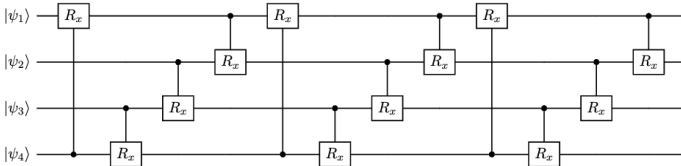


Fig. 6: Strongly entangled controlled-X CRX with circuit block connectivity interaction configuration in the proposed variational layer.

E. Optimization

Similar to classical machine learning models, the eQLSTML is trained to work with data-driven tasks. This learning process,

expressed mathematically, involves minimizing the loss function $L(\theta)$, also known as the objective function. In this paper, we used gradient-based algorithms to iteratively optimize VQC parameters. In this approach, the parameters are iteratively adjusted towards the direction that leads to the most significant decrease in the loss function, which can be expressed as:

$$\theta_j \leftarrow \theta_j - \eta \nabla_{\theta_j} L(\theta), \quad (33)$$

where ∇_{θ} is the gradient and η is the learning rate.

The parameter-shift method, a type of forward-mode automatic differentiation technique [23], was employed in the optimization procedure to calculate the analytical gradient of each VQC. The calculation for the gradient of a VQC following the parameter-shift method can be done via:

$$\nabla_{\theta} f(x, \theta) = \frac{1}{2} [f(x, \theta + \frac{\pi}{2}) - f(x, \theta - \frac{\pi}{2})], \quad (34)$$

where $f(x, \theta)$ is the output function.

The optimization process that minimizes $L(\theta)$ can be done by backpropagating the gradients between the VQCs and the classical LSTM, resulting in iterative optimization for the complete hybrid model.

F. Performance metrics

Model performances are evaluated using standard performance metrics, which includes the coefficient of determination (R^2), root mean square error (RMSE), and mean absolute error (MAE), with each metric defined by the expressions:

$$R^2 = 1 - \frac{\sum_{i=1}^N (y_i - \hat{y}_i)^2}{\sum_{i=1}^N (y_i - \bar{y})^2}, \quad (35)$$

$$RMSE = \sqrt{\frac{1}{N} \sum_{i=1}^N (y_i - \hat{y}_i)^2}, \quad (36)$$

$$MAE = \frac{1}{N} \sum_{i=1}^N |y_i - \hat{y}_i|. \quad (37)$$

G. Implementation details

The initial hyperparameter to compare the base setup for models is listed in this section. Firstly, the batch size of 512 was used for the data loader in each batch, the learning rate η is set to 0.028, the initial depth of 1, and the hidden size dimension is set to 2. The model was trained with the sequence length of 50 inputs for a window time of 2 minutes with a sampling rate chosen is 10s aggregated with standard deviation functions. All of the models, including classical LSTM and proposed eQLSTML, will be trained with 50 epochs and use early stopping for the learning process to avoid overfitting. The number of epochs is decided based on preliminary experiments which are sufficient training time for the model to converge within constraint resources and time as the model will be trained repeatedly for 11 participants. The loss function for each epoch is the average value of the total of loss for each mini-batch, divided by the total size of the batch (512 in this case). Additionally, the loss function is measured and evaluated every epoch. Lastly, the early stopper

will discontinue the learning process if the loss decreases by less than 10^{-5} for 5 consecutive epochs.

H. Training and evaluation method:

The training and testing process of our model employed the Leave One Subject Out cross validation (LOSO-CV) method to assess the generalizability of our model. In this approach, we train the model using data from all participants except for one that is reserved for the test set. This process is repeated to ensure all participants are tested separately. Moreover, the LOSO-CV is used in order to minimize potential training set leakage that can occur in standard cross-validation techniques. Lastly, to monitor the performance of the model during the training process, a validation set comprising of two participants was used. These validation sets were randomly picked for each participant but stayed consistent across all model configurations to facilitate unbiased comparison.

VII. RESULT AND DISCUSSION

This section will discuss our findings from evaluating our proposed eQLSTML model on a quantum circuit consisting of 6 qubits for the LSTM. The performance will be compared with certain cases to provide comprehensive findings on how effective our proposed models are for energy expenditure prediction.

A. Performance of classical LSTM and eQLSTML

Model performances are presented via metrics introduced in the previous section. In this comparison, test data consisted of 11 participants which performed all physical activities to aid in the models ability to focus on core functionality and overall data efficiency.

TABLE II: Evaluation metrics of 11 participants for all activities for the eQLSTML and LSTM models.

	R^2	RMSE	MAE
eQLSTML	0.77	1.27	0.93
LSTM	0.68	1.49	1.15

Table II presents the performance metric comparison between the classical LSTM model and our proposed eQLSTML model. From the scores, our proposed eQLSTML outperformed classical LSTM in terms of all evaluation metrics. Specifically, the proposed model achieved a significantly higher R^2 score of 0.77 compared to the value of $R^2 = 0.68$ from LSTM, representing a 13% improvement. In terms of RMSE and MAE, the result for LSTMs is 1.49 and 1.27, while the eQLSTML model accomplished 1.15 and 0.93, respectively. This indicates enhancements of $\sim 15\%$ for RMSE and 19% for MAE metrics. The overall results show that our proposed model not only captures the underlying relationships within the data more effectively but also can make a closer approximation of actual values.

Figure 7 presents the performed energy expenditure predictions on the data by both eQLSTML and LSTM models and the testing data of one participant (labeled GOTOV12). From

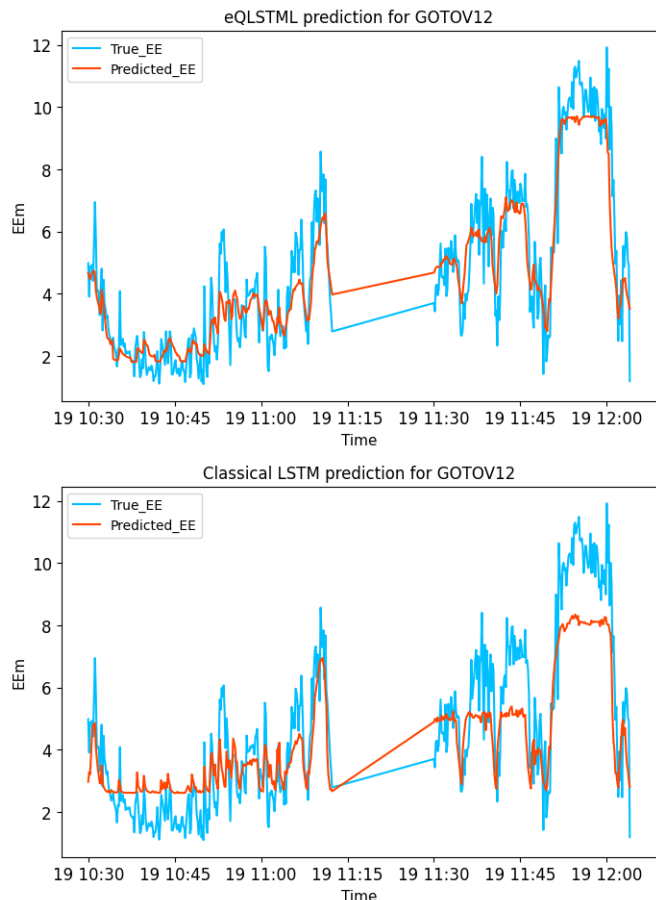


Fig. 7: True versus predicted values of EEm/breath for participant GOTOV12, with indoor and outdoor activities included, generated by our eQLSTML model (top) and the classical LSTM model (bottom).

the figure, it is clear that the prediction of the eQLSTML architecture demonstrates a remarkable capability to capture the overall trend of both long-term and short-term time-series behaviors in the unseen (test) data set and outperforms LSTM technique in predicting trends. This is easily observed when comparing the predicted and actual EEm curves between the eQLSTML and LSTM models during the time interval from 19:10:30 to 19:11:00. Furthermore, from the table III, it can be said that the proposed model also outperforms the classical architectures in all metrics when evaluated in the test dataset of GOTOV12

TABLE III: Evaluation metrics of the participant GOTOV12 for all activities for the eQLSTML and LSTM models.

	R^2	RMSE	MAE
eQLSTML	0.87	0.98	0.77
LSTM	0.74	1.37	1.13

B. Comparative analysis of model performance for indoor and outdoor activities separately

In order to make a comprehensive comparison of our eQLSTML model capability in terms of predicting low and high-intensity activities, we also evaluated the model with a

test set that includes exclusively indoor or outdoor activities and compared our results to those obtained from the classical LSTM. Table IV presents evaluation metrics for indoor activities. While the eQLSTML R^2 score is reasonably low at 0.43, it is $\sim 59\%$ higher than that obtained from the LSTM model which scored just 0.27. Additionally, we also report a favorable decrease of 13% and 18% in the RMSE and MAE metrics from the eQLSTML model, with respective scores of 0.90 and 0.67.

TABLE IV: Evaluation metrics of 11 participants for indoor activities for the eQLSTML and LSTM models.

	R^2	RMSE	MAE
eQLSTML	0.43	0.90	0.67
LSTM	0.27	1.03	0.82

Table V presents the same metric analysis from outdoor specific activities. From the tabulated data, eQLSTML performs much better when compared to indoor specific activities, with an overall R^2 of 0.60, which is 33% higher than that from the classical LSTM. Additionally, similar to the indoor specific activities, our eQLSTML model again produces smaller RMSE and MAE scores compared with LSTM, with reported decreases of $\sim 16\%$ and 18%, respectively.

TABLE V: Evaluation metrics of 11 participants for outdoor activities for the eQLSTML and LSTM models.

	R^2	RMSE	MAE
eQLSTML	0.60	1.61	1.26
LSTM	0.45	1.91	1.54

C. Performance comparison of encoding techniques

We next present the performance metrics of our eQLSTML model when employing angle, 2Nr, and amplitude embedding techniques. Table VI presents the comparative results of each encoding technique using both indoor and outdoor participant data. In these experiments, the variational layer in each case incorporated CRX gates and the circuit size was fixed to include 6 qubits. From the tabulated data, it is clear that the use of angle embedding consistently outperformed the other encoding techniques. Collectively, it has the highest performing values in R^2 , RMSE and MAE, with respective values of 0.77, 1.27, and 0.93, which represent a 11%, 14%, and 16% performance increase when compared to 2Nr, the second highest performing technique.

TABLE VI: Comparison of performance metrics for our eQLSTML model utilizing different encoding techniques on a 6 qubit circuit which utilized CRX gates in the variational layer.

Technique	R^2	RMSE	MAE
Angle	0.77	1.27	0.93
2Nr	0.69	1.47	1.11
Amplitude	0.67	1.53	1.15

We also performed experiments comparing the three encoding techniques for specific indoor (i) and outdoor (o) activities

with the resulting performance metrics for each case shown in Table VII. Interestingly, the use of angle embedding in indoor activities resulted in a significant improvement in iR^2 , with a 37% increase compared to amplitude encoding, the second highest performance technique, as well as additional performance improvements of 13% in $iRMSE$ and 14% in $iMAE$. For outdoor-specific activities, heightened performance were again witnessed across all three performance metrics associated with using angle embedding, however, 2Nr encoding performed more favorably over amplitude encoding. As seen in the table, oR^2 , $oRMSE$, and $oMAE$ from angle encoding showed increases of 18%, 12%, and 14%, respectively, when compared to 2Nr.

TABLE VII: Comparison of performance metrics for difference encoding techniques for indoor (i) and outdoor (o) specific activities.

Technique	iR^2	oR^2	$iRMSE$	$oRMSE$	$iMAE$	$oMAE$
Angle	0.43	0.60	0.90	1.61	0.67	1.26
2Nr	0.19	0.49	1.09	1.82	0.83	1.46
Amplitude	0.27	0.42	1.03	1.96	0.78	1.60

The angle embedding technique is likely more effective than both 2Nr encoding and amplitude encoding for this specific dataset due to the way it handles data representation. A possible explanation for the inferior performance of 2Nr encoding is its use of the arctan transformation, which compresses larger data values but distorts the natural range and relationships in the data. This compression is not ideal for temporal data modeling, where preserving the variability and dynamics of the dataset is crucial for performance. On the other hand, amplitude encoding, while efficient for encoding high-dimensional data (up to 64 features with 6 qubits), may be too complicated for a dataset with only 6 features. The unused feature space can introduce inefficiencies and noise, making the encoding less optimal. In contrast, angle embedding provides a direct and efficient way to encode each feature into qubit rotations, preserving the structure and ensuring more effective use of the quantum circuit's capacity, which is better suited for smaller feature sets.

D. Rotational gates comparison analysis

We also conducted experiments comparing the performance of different entangling gates, namely CNOT, CRZ, and CRX gates, implemented in the variational layer of our eQLSTML model. We present the resulting performance metrics in Table VIII. To make a fair comparison, all experiments were conducted on a 6-qubit circuit and employing angle embedding based on its superior performance highlighted in the previous section.

TABLE VIII: Resulting performance metrics from experiments utilizing different entangling gates.

Gates	R^2	RMSE	MAE
CRX	0.77	1.27	0.93
CRZ	0.74	1.34	0.99
CNOT	0.70	1.47	1.12

From the data in Table VIII, we see that the implementation of the CRX gate offers a moderate increase in the models ability to capture complex temporal dependencies when compared to the CRZ and CNOT gates, with the latter showing the lowest performance. Specifically, the CRX gate implementation achieved the highest R^2 of 0.77, and lower RMSE and MAE values which were found to be 1.27 and 1.61, respectively, indicating its superior accuracy in both training and testing phases. Furthermore, the implementation of the CRZ gate, while competitive with $R^2 = 0.74$, slightly underperforms when compared to CRX implementation, with higher RMSE and MAE values of 1.34 and 1.69, respectively.

TABLE IX: Comparison of performance metrics across different encoding techniques indoor and outdoor activity performance.

Technique	iR^2	oR^2	iRMSE	oRMSE	iMAE	oMAE
CRX	0.43	0.60	0.90	1.61	0.67	1.26
CRZ	0.37	0.55	0.96	1.69	0.72	1.33
CNOT	0.24	0.47	1.06	1.85	0.82	1.49

We again look at the performance output of each gate implementation in the variational layer for outdoor and indoor-specific activities, with metrics presented in Table IX. As seen in the table, the use of the CRX gate results in the best performance among the three gate choices we investigated for both indoor and outdoor activities. Use of the CRZ gate also performed well, with values for R^2 , RMSE, and MAE only approximately 5% – 16% less than those obtained when using CRX gates in our experiments for both indoor and outdoor activities. Lastly, the use of the CNOT gate resulted in the lowest scores for all metrics in both indoor and outdoor activities, with a particularly low iR^2 value of 0.24, 44% lower than that from using the CRX gates.

Overall, the CRX gate proves to be the optimal choice, offering the best balance between performance and training speed, whereas CRZ remains a viable alternative but with slightly slower training times. CNOT, due to its limited expressibility as well as its fixed operation, is less suited for use in PAEE estimation and prediction.

E. Linear embedding layer types

To confirm our expectation that separate linear embedding before and after each VQC is a better configuration, we also performed an experiment with two configurations of the linear embedding layers we called Shared-Separate and Separate-Separate. The results of these experiments are shown in Table X and indicate a minor but improved performance in the Separate-Separate configuration, with 6%, 9%, and 11% improvements in R^2 , RMSE, and MAE values, respectively, compared to the Shared-Separate case. Collectively, these findings imply the Separate-Separate approach is able to handle larger data variance more efficiently, which suggests a higher predictive power.

Table XI presents the performance metrics when utilizing the Shared-Separate and Separate-Separate approaches for indoor and outdoor-specific activities. From the data,

TABLE X: Overall performance metrics from the Shared-Separate and Separate-Separate linear embedding approaches.

Types	R^2	RMSE	MAE
Shared-Separate	0.72	1.39	1.04
Separate-Separate	0.77	1.27	0.93

the Separate-Separate approach performs much better than Shared-Separate for indoor-specific activities, with an impressive 60% increase in R^2 . Performance using the Separate-Separate approach also yields smaller, but improvable performance metrics for outdoor-specific activities, with 8%-12% improvement in oR^2 , $oRMSE$, and $oMAE$.

Given these results, the Separate-Separate configuration is clearly the optimal choice for embedding in PAEE estimation and prediction. This configuration allows for better handling of the input and output information within the VQC layers which leads to an overall improved learning and generalization, as supported by the performance metrics.

TABLE XI: Comparison of performance metrics across different encoding techniques indoor and outdoor activity performance.

Technique	iR^2	oR^2	iRMSE	oRMSE	iMAE	oMAE
Separate/Separate	0.43	0.60	0.90	1.61	0.67	1.26
Shared/Separate	0.17	0.53	1.10	1.75	0.84	1.38

F. Model performance with lower qubit usage

TABLE XII: Evaluation metrics of overall performance metrics for different numbers of qubits using the Separate-Separate embedding approach.

Number of qubits	R^2	RMSE	MAE
4qubits	0.76	1.30	0.97
6qubits	0.77	1.27	0.93

To assess the model’s performance and verify its robustness under constrained quantum resources, we conducted a comparative analysis by reducing the number of qubits from 6 to 4, with performance metrics for both experiments shown in Table XII. As shown in the data, reducing the number of qubits from 6 to 4 results in nearly identical performances, indicating that fewer qubits still allow our model to effectively capture variance and retain prediction accuracy. Overall, the minimal decline in performance highlights the robustness of the Separate-Separate embedding configuration and its need for fewer resources.

G. Summary of key findings

- **Best Encoding Technique:** Among the tested encoding methods, angle embedding clearly stood out, delivering significantly better results than 2Nr and amplitude encoding. This is likely because angle embedding effectively preserves the original structure of the data and fully leverages the capacity of quantum circuits, making it particularly suitable for tasks involving relatively small feature sets.

- **Optimal Gate Choice:** We found that using CRX gates consistently improved performance over CRZ and CNOT gates. This improvement is mainly due to CRX gates' enhanced ability to create stronger entanglements and more thoroughly explore quantum states, thereby boosting the model's overall capability.
- **Embedding Layer Configuration:** The Separate-Separate configuration, using distinct linear embedding layers before and after each VQC block, provided better results than sharing embedding layers. This approach notably enhanced the model's ability to capture subtle variations in the data, ultimately improving predictive accuracy.
- **Quantum Resource Efficiency:** Interestingly, reducing the number of qubits from six to four did not significantly affect performance. This suggests that our proposed model remains robust even when quantum resources are limited, highlighting practical feasibility and efficiency.

VIII. CONCLUSION

In this study, we proposed a hybrid quantum-classical machine learning model, named enhanced Quantum Long Short-Term Memory Linear (eQLSTML), for predicting physical activity energy expenditure (PAEE) in older individuals. By leveraging quantum computing capabilities, specifically integrating variational quantum circuits (VQCs) within LSTM frameworks. Our approach has demonstrated improved predictive accuracy and efficiency compared to classical LSTM models. The experimental results showed substantial improvements in predictive accuracy, as evidenced by superior evaluation metrics, including increased R^2 values, as well as reduced RMSE and MAE scores across various indoor and outdoor physical activities. The eQLSTML model's utilization of angle embedding techniques, separate linear embedding layers, and variational quantum circuits with strongly entangled controlled-X (CRX) gates enabled more effective handling of complex temporal dependencies and reduced computational demands. Collectively, these improvements illustrate the significant potential of quantum-enhanced machine learning methods to provide superior performance compared to classical methods, particularly within the healthcare and IoT monitoring domains.

While our findings indicate promising outcomes for quantum-enhanced prediction and estimation of PAEE in elderly healthcare, further research is necessary. Several promising areas remain open for future work. First, our immediate plan involves integrating the proposed quantum models with real quantum hardware to validate model performance under realistic quantum computing conditions. This will potentially require upgraded and modified versions of our proposed framework and eQLSTML model to enable practical deployment on real quantum hardware, addressing challenges related to hardware integration, limited qubit coherence, and scalability. Additionally, future work should specifically explore incorporating quantum error correction and fault-tolerance mechanisms into quantum-enhanced neural

networks to achieve robust and reliable model training and inference in the presence of quantum noise inherent to noisy intermediate-scale quantum (NISQ) devices. Moreover, deeper exploration of advanced hybrid quantum-classical optimization algorithms may further enhance training efficiency and reduce computational complexity. This direction could facilitate faster model convergence and enable efficient training procedures suitable for large-scale, real-time healthcare applications. Addressing these future research directions promises considerable progress toward practical, reliable, and highly accurate quantum machine learning implementations. Ultimately, these advancements will substantially reinforce the application of quantum machine learning methodologies in healthcare which fosters significant improvements in personalized health monitoring and predictive healthcare analytics and contributes meaningfully toward promoting healthy and active aging.

ACKNOWLEDGMENT

This work was supported in part by the Canada Excellence Research Chair (CERC) Program CERC-2022-00109. The work of H. Shin was supported by the National Research Foundation of Korea (NRF) grant funded by the Korean government (MSIT) under RS-2025-00556064 and by the MSIT (Ministry of Science and ICT), Korea, under the Convergence security core talent training business support program (RS-2023-00266615) supervised by the IITP (Institute for Information & Communications Technology Planning & Evaluation).

REFERENCES

- [1] M. N. Bhuiyan, M. M. Rahman, M. M. Billah, and D. Saha, "Internet of things (IoT): A review of its enabling technologies in healthcare applications, standards protocols, security, and market opportunities," *IEEE Internet of Things Journal*, vol. 8, no. 13, pp. 10474–10498, 2021.
- [2] J. Chen, Y. Shi, C. Yi, H. Du, J. Kang, and D. Niyato, "Generative-AI-driven human digital twin in IoT healthcare: A comprehensive survey," *IEEE Internet of Things Journal*, vol. 11, no. 21, pp. 34749–34773, 2024.
- [3] A. Alqahtani, S. Alsubai, and M. Bhatia, "Digital-twin-assisted healthcare framework for adult," *IEEE Internet of Things Journal*, vol. 11, no. 8, pp. 14963–14970, 2024.
- [4] A. Botosaneanu, S. Markwardt, and A. R. Quiñones, "Multimorbidity and functional disability among older adults: The role of inflammation and glycemic status – an observational longitudinal study," *Gerontology*, vol. 69, no. 7, p. 826–838, Jul. 2023.
- [5] W. Ahmed, T. Muhammad, and K. Muneera, "Prevalence of early and late onset of chronic diseases and multimorbidity and its association with physical, mental and functional health among older Indian adults," *BMC Geriatrics*, vol. 23, p. Article number: 563, 2023.
- [6] M. Nystoriak and A. Bhatnagar, "Cardiovascular effects and benefits of exercise," *Frontiers in Cardiovascular Medicine*, vol. 5, p. Article 135, 2018.
- [7] S. Chastin, U. Abaraogu, J. Bourgois, P. Dall, J. Darnborough, E. Duncan, J. Dumortier, D. J. Pavón, J. McParland, N. Roberts, and M. Hamer, "Effects of regular physical activity on the immune system, vaccination and risk of community-acquired infectious disease in the general population: Systematic review and meta-analysis," *Sports Medicine*, vol. 51, pp. 1673–1686, 2021.
- [8] J. Lacombe, M. Armstrong, F. L. Wright, and C. Foster, "The impact of physical activity and an additional behavioural risk factor on cardiovascular disease, cancer and all-cause mortality: A systematic review," *BMC Public Health*, vol. 19, p. Article 7030, 2019.
- [9] T. M. Manini, J. E. Everhart, K. V. Patel, D. A. Schoeller, L. H. Colbert, M. Visser, F. Tyllavsky, D. C. Bauer, B. H. Goodpaster, and T. B. Harris, "Daily activity energy expenditure and mortality among older adults," *JAMA*, vol. 296, no. 2, pp. 171–179, 2006.

- [10] A. Chaddad, Y. Wu, and C. Desrosiers, "Federated learning for healthcare applications," *IEEE Internet of Things Journal*, vol. 11, no. 5, pp. 7339–7358, 2024.
- [11] H. Elayan, M. Aloqaily, and M. Guizani, "Digital twin for intelligent context-aware IoT healthcare systems," *IEEE Internet of Things Journal*, vol. 8, no. 23, pp. 16749–16757, 2021.
- [12] W. R. Leonard, "Laboratory and field methods for measuring human energy expenditure," *American Journal of Human Biology*, vol. 24, no. 3, pp. 372–384, 2012.
- [13] A. H. K. Montoye, M. Begum, Z. Henning, and K. A. Pfeiffer, "Comparison of linear and non-linear models for predicting energy expenditure from raw accelerometer data," *Physiological Measurement*, vol. 38, no. 2, p. 343, jan 2017.
- [14] S. Paraschiakos, C. R. de Sá, J. Okai, P. E. Slagboom, M. Beekman, and A. Knobbe, "A recurrent neural network architecture to model physical activity energy expenditure in older people," *Data Min Knowl Disc* 36, 2022.
- [15] N. Caron, N. Peyrot, T. Caderby, C. Verkindt, and G. Dalleau, "Estimating energy expenditure from accelerometer data in healthy adults and patients with type 2 diabetes," *Experimental Gerontology*, vol. 134, p. 110894, 2020.
- [16] S. B. Roberts and G. E. Dallal, "Energy requirements and aging," *Public Health Nutrition*, vol. 8, no. 7a, pp. 1028–1036, 2005.
- [17] T. Hortobágyi, C. Mizelle, S. Beam, and P. DeVita, "Old adults perform activities of daily living near their maximal capabilities," *The Journals of Gerontology: Series A*, vol. 58, no. 5, pp. M453–M460, 2003.
- [18] M. I. Frisard, A. Broussard, S. S. Davies, I. Roberts, L. Jackson, J. Rood, L. de Jonge, X. Fang, S. M. Jazwinski, W. A. Deutsch, and E. Ravussin, "Aging, resting metabolic rate, and oxidative damage: Results from the louisiana healthy aging study," *The Journals of Gerontology: Series A*, vol. 62, no. 7, pp. 752–759, 2007.
- [19] J. D. Knaggs, K. A. Larkin, and T. M. Manini, "Metabolic cost of daily activities and effect of mobility impairment in older adults," *Journal of the American Geriatrics Society*, vol. 59, no. 11, pp. 2118–2123, 2011.
- [20] A. J. van Ballegooijen, H. P. van der Ploeg, and M. Visser, "Daily sedentary time and physical activity as assessed by accelerometry and their correlates in older adults," *European Review of Aging and Physical Activity*, vol. 16, p. Article number: 3, 2019.
- [21] G. Wendin, "Quantum information processing with superconducting circuits: a review," *Reports on Progress in Physics*, vol. 80, no. 10, Sep. 2017.
- [22] I. Cong, S. Choi, and M. D. Lukin, "Quantum convolutional neural networks," *Nature Physics*, vol. 15, no. 12, pp. 1273–1278, 2019.
- [23] K. Mitarai, M. Negoro, M. Kitagawa, and K. Fujii, "Quantum circuit learning," *Phys. Rev. A*, vol. 98, p. 032309, Sep 2018.
- [24] A. Ceschini, A. Rosato, and M. Panella, "Hybrid quantum-classical recurrent neural networks for time series prediction," in *2022 International Joint Conference on Neural Networks (IJCNN)*, Italy, 2022, pp. 1–8.
- [25] Y. Cao, X. Zhou, X. Fei, H. Zhao, W. Liu, and J. Zhao, "Linear-layer-enhanced quantum long short-term memory for carbon price forecasting," *Quantum Machine Intelligence*, vol. 5, jul 2023.
- [26] J. Bausch, "Recurrent quantum neural networks," in *Advances in Neural Information Processing Systems*, H. Larochelle, M. Ranzato, R. Hadsell, M. Balcan, and H. Lin, Eds., vol. 33. Curran Associates, Inc., 2020, pp. 1368–1379.
- [27] V. Gandhi, G. Prasad, D. Coyle, L. Behera, and T. M. McGinnity, "Quantum neural network-based eeg filtering for a brain-computer interface," *IEEE Transactions on Neural Networks and Learning Systems*, vol. 25, no. 2, pp. 278–288, 2014.
- [28] S. Y.-C. Chen, S. Yoo, and Y.-L. L. Fang, "Quantum long short-term memory," in *IEEE International Conference on Acoustics, Speech and Signal Processing (ICASSP)*, 2022.
- [29] A. Ceschini, A. Rosato, and M. Panella, "Design of an lstm cell on a quantum hardware," *IEEE Transactions on Circuits and Systems II: Express Briefs*, vol. 69, no. 3, pp. 1822–1826, 2022.
- [30] C.-H. A. Lin, C.-Y. Liu, and K.-C. Chen, "Quantum-train long short-term memory: Application on flood prediction problem," in *2024 IEEE International Conference on Quantum Computing and Engineering (QCE)*, vol. 02, 2024, pp. 268–273.
- [31] M. Chehimi, S. Y. C. Chen, and W. Saad, "Federated quantum long short-term memory (fedqlstm)," *Quantum Machine Intelligence*, vol. 6, no. 1, p. 43, 2024.
- [32] M. Schuld, R. Sweke, and J. J. Meyer, "Effect of data encoding on the expressive power of variational quantum-machine-learning models," *Physical Review A*, vol. 103, no. 3, p. 032430, 2021.
- [33] Y. Cao, G. G. Guerreschi, and A. Aspuru-Guzik, "Quantum neuron: an elementary building block for machine learning on quantum computers," *arXiv preprint arXiv:1711.11240*, 2017.
- [34] K. Ellis, J. Kerr, S. Godbole, G. Lanckriet, D. Wing, and S. Marshall, "A random forest classifier for the prediction of energy expenditure and type of physical activity from wrist and hip accelerometers." *Physiol Meas*, Oct. 2014.
- [35] J. Staudenmayer, D. Pober, S. Crouter, D. Bassett, and P. Freedson, "An artificial neural network to estimate physical activity energy expenditure and identify physical activity type from an accelerometer," *Journal of Applied Physiology*, vol. 107, no. 4, pp. 1300–1307, 2009.
- [36] J. Zhu, A. Pande, P. Mohapatra, and J. J. Han, "Using deep learning for energy expenditure estimation with wearable sensors," in *2015 17th International Conference on E-health Networking, Application Services (HealthCom)*, Boston, USA, 2015, pp. 501–506.
- [37] S. Aishwarya, V. Abeer, B. B. Sathish, and K. Subramanya, "Quantum computational techniques for prediction of cognitive state of human mind from eeg signals," *Journal of Quantum Computing*, vol. 2, no. 4, pp. 157–170, 2020.
- [38] S. S. Kavitha and N. Kaulgud, "Quantum k-means clustering method for detecting heart disease using quantum circuit approach," *Soft Computing*, pp. 1–14, 2022.
- [39] P. Kairon and S. Bhattacharyya, *COVID-19 Outbreak Prediction Using Quantum Neural Networks*, 01 2021, pp. 113–123.
- [40] S. Paraschiakos, R. Cachucho, M. Moed, D. van Heemst, S. Mooijaart, E. P. Slagboom, A. Knobbe, and M. Beekman, "Activity recognition using wearable sensors for tracking the elderly," *User Modeling and User-Adapted Interaction*, vol. 30, no. 3, pp. 567–605, 2020.
- [41] S. Paraschiakos, C. R. de Sá, J. Okai, P. E. Slagboom, M. Beekman, and A. Knobbe, "A recurrent neural network architecture to model physical activity energy expenditure in older people," *Data Mining and Knowledge Discovery*, vol. 36, no. 1, p. 477–512, Jan. 2022. [Online]. Available: <http://dx.doi.org/10.1007/s10618-021-00817-w>
- [42] B. B. Parr, S. J. Strath, D. Bassett, and E. T. Howley, "Validation of the cosmed k4 b2 portable metabolic system," *Int J Sports Med*, vol. 22, pp. 280–284, 2001.
- [43] W. Gerrish and J. Schmidhuber, "Standardizing neural network inputs from preferential activation functions," in *Proceedings of the 13th International Conference on Artificial Neural Networks*. Springer-Verlag, 2010, pp. 161–166.
- [44] G. James, D. Witten, T. Hastie, and R. Tibshirani, *An Introduction to Statistical Learning with Applications in R*. Springer Science Business Media, 2013.
- [45] T. Jayalakhshmi and A. Santhakumaran, "Statistical normalization and back propagation for classification," *International Journal of Computer Theory and Engineering*, vol. 3, no. 1, pp. 1793–8201, 2011.
- [46] D. Singh and B. Singh, "Investigating the impact of data normalization on classification performance," *Applied Soft Computing*, vol. 97, p. 105524, 2020.
- [47] M. A. Nielsen and I. L. Chuang, *Quantum Computation and Quantum Information: 10th Anniversary Edition*. Cambridge University Press, 2010.
- [48] S. Sim, P. D. Johnson, and A. Aspuru-Guzik, "Expressibility and entangling capability of parameterized quantum circuits for hybrid quantum-classical algorithms," *Advanced Quantum Technologies*, vol. 2, no. 12, p. 1900070, 2019.
- [49] Y. Liu, K. Baba, K. Kaneko, N. Takeda, J. Koyama, and K. Kimura, "Analysis of parameterized quantum circuits: on the connection between expressibility and types of quantum gates," 2024.
- [50] M. Cerezo, A. Arrasmith, R. Babbush, S. C. Benjamin, S. Endo, K. Fujii, J. R. McClean, K. Mitarai, X. Yuan, L. Cincio, and P. J. Coles, "Variational quantum algorithms," *Nature Reviews Physics*, vol. 3, pp. 625 – 644, Aug. 2020.
- [51] M. Benedetti, E. Lloyd, S. Sack, and M. Fiorentini, "Parameterized quantum circuits as machine learning models," *Quantum Science and Technology*, vol. 4, no. 4, p. 043001, Nov. 2019.
- [52] S. McArdle, S. Endo, A. Aspuru-Guzik, S. C. Benjamin, and X. Yuan, "Quantum computational chemistry," *Reviews of Modern Physics*, vol. 92, Mar. 2020.
- [53] P.-L. Dallaire-Demers and N. Killoran, "Quantum generative adversarial networks," *Phys. Rev. A*, vol. 98, p. 012324, Jul. 2018.
- [54] S. E. Gaily and S. Imre, "Quantum optimization in large resource management systems," in *2019 IEEE 20th International Workshop on Signal Processing Advances in Wireless Communications (SPAWC)*, 2019.

- [55] Y. Du, M.-H. Hsieh, T. Liu, and D. Tao, “Expressive power of parametrized quantum circuits,” *Phys. Rev. Res.*, vol. 2, p. 033125, Jul. 2020.
- [56] T. Lanting, A. J. Przybysz, A. Y. Smirnov, F. M. Spedalieri, M. H. Amin, A. J. Berkley, R. Harris, F. Altomare, S. Boixo, P. Bunyk, N. Dickson, C. Enderud, J. P. Hilton, E. Hoskinson, M. W. Johnson, E. Ladizinsky, N. Ladizinsky, R. Neufeld, T. Oh, I. Perminov, C. Rich, M. C. Thom, E. Tolkacheva, S. Uchaikin, A. B. Wilson, and G. Rose, “Entanglement in a quantum annealing processor,” *Phys. Rev. X*, vol. 4, p. 021041, May 2014.
- [57] S. Hochreiter and J. Schmidhuber, “Long short-term memory,” *Neural Comput.*, vol. 9, no. 8, p. 1735–1780, nov 1997.
- [58] I. Sutskever, O. Vinyals, and Q. V. Le, “Sequence to sequence learning with neural networks,” in *Proceedings of the 27th International Conference on Neural Information Processing Systems - Volume 2*, ser. NIPS’14, 2014, p. 3104–3112.
- [59] Y. Wang, M. Huang, X. Zhu, and L. Zhao, “Attention-based LSTM for aspect-level sentiment classification,” in *Proceedings of the 2016 Conference on Empirical Methods in Natural Language Processing*, Austin, Texas, Nov. 2016, pp. 606–615.
- [60] F. Karim, S. Majumdar, H. Darabi, and S. Chen, “Lstm fully convolutional networks for time series classification,” *IEEE Access*, vol. 6, pp. 1662–1669, 2018.
- [61] C. Olah, “Understanding lstm networks,” *colah.github.io*, 2015.
- [62] E. Ovalle-Magallanes, D. E. Alvarado-Carrillo, J. G. Avina-Cervantes, I. Cruz-Aceves, and J. Ruiz-Pinales, “Quantum angle encoding with learnable rotation applied to quantum-classical convolutional neural networks,” *Applied Soft Computing*, vol. 141, p. 110307, 2023.
- [63] M. Schuld and F. Petruccione, *Supervised Learning with Quantum Computers*, ser. Quantum Science and Technology. Springer Cham, 2018.
- [64] E. Ovalle-Magallanes, D. E. Alvarado-Carrillo, J. G. Avina-Cervantes, I. Cruz-Aceves, and J. Ruiz-Pinales, “Quantum angle encoding with learnable rotation applied to quantum-classical convolutional neural networks,” *Applied Soft Computing*, vol. 141, 2023.